

Noninvasive magnetic detection of 2D van der Waals room-temperature ferromagnet Fe₃GaTe₂ using divacancy spins in SiC

Xia Chen^{1,†}, Qin-Yue Luo^{1,†}, Pei-Jie Guo¹, Hao-Jie Zhou¹, Qi-Cheng Hu¹, Hong-Peng Wu^{2,3}, Xiao-Wen Shen^{2,3}, Ru-Yue Cui^{2,3}, Lei Dong^{2,3}, Tian-Xing Wei¹, Yu Hang Xiao¹, De-Ren Li¹, Li Lei⁴, Xi Zhang¹, Jun-Feng Wang^{1,*}, Gang Xiang^{1,*}

¹College of Physics, Sichuan University, Chengdu 610065, China

²State Key Laboratory of Quantum Optics and Quantum Optics Devices, Institute of Laser Spectroscopy, Shanxi University, Taiyuan 030006, China

³Collaborative Innovation Center of Extreme Optics, Shanxi University, Taiyuan 030006, China

⁴Institute of Atomic and Molecular Physics, Sichuan University, Chengdu 610065, China

[†]These authors contributed equally: Xia Chen, Qin-Yue Luo.

*Corresponding author: jfwang@scu.edu.cn; gxiang@scu.edu.cn

Abstract

Room-temperature (RT) two-dimensional (2D) van der Waals (vdW) ferromagnets hold immense promise for next-generation spintronic devices for information storage and processing. To achieve high-density energy-efficient spintronic devices, it is essential to understand local magnetic properties of RT 2D vdW magnets. In this work, we realize noninvasive *in situ* magnetic detection in vdW-layered ferromagnet Fe₃GaTe₂ using divacancy spins quantum sensor in silicon carbide (SiC) at RT. The structural features and magnetic properties of the Fe₃GaTe₂ are characterized utilizing Raman spectrum, magnetization and magneto-transport measurements. Further detailed analysis of temperature- and magnetic field-dependent optically detected magnetic resonances of the PL6 divacancy near the Fe₃GaTe₂ reveal that, the Curie temperature (T_c) of Fe₃GaTe₂ is ~ 360 K, and the magnetization increases with external magnetic fields. Additionally, spin relaxometry technology is employed to probe the magnetic fluctuations of Fe₃GaTe₂, revealing a peak in the spin relaxation rate around the T_c . These experiments give insights into the intriguing local magnetic properties of 2D vdW RT ferromagnet Fe₃GaTe₂ and pave the way for the application of SiC quantum sensors in noninvasive *in situ* magnetic detection of related 2D vdW magnets.

Introduction

In recent years, numerous innovative magnetic materials such as van der Waals (vdW) magnets¹, topological insulators² and high-temperature superconductors³ have been discovered and drawn extensive attention¹⁻⁵. Among those, various vdW ferromagnetic materials have emerged as promising platforms for two-dimensional (2D) high-density low-power spintronic devices due to their remarkable properties, including high degrees of freedom encompassing spin, charge and intrinsic magnetism⁶⁻⁸. However, a common limitation faced by most 2D vdW ferromagnets lies in their low Curie temperatures (T_c), which restricts their practical applications in spintronic devices⁶⁻¹⁰. Recently, the discovery of room-temperature (RT) vdW ferromagnet Fe_3GaTe_2 has captured significant interest due to its robust intrinsic ferromagnetism^{9,10}.

The growing novel magnetic materials inspire scientists to develop new technologies to investigate the local magnetic fields generated by spins and electric currents in these materials^{4,5,11}. Traditional magnetic field detection technologies, such as nuclear magnetic resonance (NMR) and magnetic force microscopy (MFM), have played crucial roles in studying magnetic materials. However, these methods suffer from limitations, including poor spatial resolution, narrow operating temperature ranges, and perturbative effects from magnetic probes^{4,5}. To address these challenges, some spin qubits in solid-state including nitrogen-vacancy (NV) centers in diamond and boron vacancy (V_B^-) defects in hexagonal boron nitride (hBN) have been exploited as versatile magnetic quantum sensors^{4,5,12-14}. Owing to the advantages of noninvasive, high sensitivity, nanoscale spatial resolution and wide operating temperature range, spin qubits have been applied for detecting static and dynamic magnetic field in various materials, encompassing ferromagnetic materials, superconductors, and topological insulators, even under high pressure^{4,5,12-15}. However, integrating these spin qubits with practical electronic devices is still of great challenge. The diamond and hBN substrates lack mature growth and micro/nano fabrication process as well as compatibility with complementary metal-oxide-semiconductor (CMOS) technology. Fortunately, recent accomplishments have highlighted silicon carbide (SiC) as a promising solid-state system for quantum technologies¹⁶⁻²². SiC is a mature semiconductor, characterized by well-established inch scale single-crystalline growth and subsequent doping and device fabrication protocols¹⁶⁻²². Moreover, SiC enjoys widespread adoption in high-power electronic devices, making it an ideal candidate for integration with 2D vdW ferromagnetic materials in spintronic and electronic applications.

The spin qubits in SiC, including silicon vacancy, divacancy, NV centers and transition-metal color centers¹⁶⁻²³, have been exploited in quantum photonics, quantum information processing, quantum network and quantum sensing due to their near infrared fluorescence and remarkable coherence properties, even at RT¹⁹⁻²³. In the realm of quantum sensing, these spin qubits serve as robust and versatile nanoscale sensors, capable of measuring various physical quantities such as magnetic fields, electric fields, strain, pressure, and temperature^{19-22,24-29}. For instance, nanotesla magnetometry have been realized using optically detected magnetic resonance (ODMR) technologies of the silicon vacancy ensemble²⁴. Additionally, SiC-based anvil cells enable the *in situ* magnetic detections for superconductors under high pressure²⁵. The charge states and ODMR approaches of divacancies have been applied to realize electric field sensing^{26,27}. High-sensitivity temperature sensing (14 mK/Hz^{1/2}) is also realized through the utilization of thermal dynamical decoupling methods²⁸. Recently, divacancies in SiC have exhibited wide-range pressure sensing capabilities with a sensitivity of 0.28 MPa/Hz^{1/2} at RT²⁹. Despite these advances, most quantum sensing concentrates on probing various physical quantities, while little is applied to probe magnetic properties in condensed matter physics^{19-22,24-29}. By leveraging SiC's mature technologies, we can expand the scope of SiC-based quantum sensing and accelerate the development of vdW ferromagnet-based spintronic and electronic devices.

In this work, we achieve the noninvasive *in situ* local magnetic detection of the 2D vdW-layered Fe₃GaTe₂ using divacancy spins in SiC at RT, where a layer of shallow divacancies serves as the local magnetic probes of small pieces of Fe₃GaTe₂ flakes. The lattice vibration, magnetization and anomalous Hall resistance properties of the Fe₃GaTe₂ sample are firstly characterized. We then compare the temperature-dependent ODMR signals from divacancies located near and far from the Fe₃GaTe₂ sample, and reveal that the T_c of Fe₃GaTe₂ is ~ 360 K. Additionally, the magnetic field-dependent ODMR signals are measured to study the evolution of magnetization with magnetic field. Finally, a peak in the spin relaxation rate around the T_c is discovered through the temperature-dependent spin relaxometry. These experiments lay the groundwork for the applications of mainstream semiconductor technology-friendly SiC-based quantum sensors to noninvasive *in situ* local magnetic detection of 2D vdW ferromagnets.

Results

The lattice vibration, elemental composition and stoichiometry measurements are

first performed to identify the Fe₃GaTe₂ sample. Fig. 1a. illustrates the crystalline structure of Fe₃GaTe₂. The vdW-layered Fe₃GaTe₂ presents a hexagonal structure ($a=b=3.99 \text{ \AA}$, $c=16.23 \text{ \AA}$, $\alpha=\beta=90^\circ$, $\gamma=120^\circ$) with $p6_3/mmc$ space group, where each Fe₃Ga layer is encapsulated by two Te layers and the adjacent 0.78-nm-thick Te layers are bonded by weak vdW force³⁰. The Raman spectroscopy of the vdW-layered Fe₃GaTe₂ in Fig. 1c. shows two prominent Raman peaks at 125.8 cm^{-1} and 143.0 cm^{-1} under a 25 mW excitation laser, corresponding to the A_{1g} and E_{2g} vibrational modes of Fe₃GaTe₂³¹, respectively. The absence of extraneous peaks corroborates the high crystal quality of the Fe₃GaTe₂ sample. The scanning electron microscope (SEM) picture and the correlated energy dispersive X-ray spectroscopy (EDS) mapping in Fig. 1d. indicate that, the flattened Fe₃GaTe₂ sample exhibits a uniform elemental distribution and a moderate atomic ratio of Fe, Ga and Te elements is 3.14:1.00:1.97, well consistent with the stoichiometric ratio.

Then, the intriguing RT ferromagnetic properties are examined by a magnetic properties measurement system (MPMS, Quantum Design). Fig. 1e. presents the out-of-plane (OP) and in-plane (IP) temperature-dependent magnetization curves under zero-field cooling (ZFC) and field-cooling (FC) conditions, exhibiting a typical magnetic phase transition from paramagnetism to ferromagnetism at the T_c of $\sim 360 \text{ K}$, consistent with the reported T_c of single-crystalline Fe₃GaTe₂ samples^{9,31}. An apparent preponderance on OP magnetization than IP one indicates the perpendicular magnetic anisotropy (PMA) in the Fe₃GaTe₂. The RT ferromagnetism and PMA in the Fe₃GaTe₂ are also explicitly implied by magnetic field-dependent OP and IP magnetization ($M-H$) curves at 300 K, as shown in Fig. 1f. Meanwhile, the magnetic domain structures are characterized by magnetic force microscopy (MFM) at RT in the absence of external magnetic field (details can be seen in Supplementary S1), which reveals the occurrence of a single- (multi-) domain state in thin (thick) Fe₃GaTe₂ flakes due to the competition among dipole interaction, exchange interaction and magnetic anisotropy³¹, underscoring the robust RT ferromagnetism of the Fe₃GaTe₂.

Since the well-established RT PMA of the Fe₃GaTe₂ can also be confirmed by magneto-transport properties, next, longitudinal resistivity (ρ_{xx}) and transverse resistivity (ρ_{xy}) of the Fe₃GaTe₂-based Hall bar device are conducted (fabrication details can be seen in Supplementary S2). Figs. 1g, h, present the temperature-dependent ρ_{xx} , where the ρ_{xx} decreases with decreasing temperature, revealing the metal conducting behavior of the Fe₃GaTe₂ nanoflake. Interestingly, the inflection point of the ρ_{xx} occurs

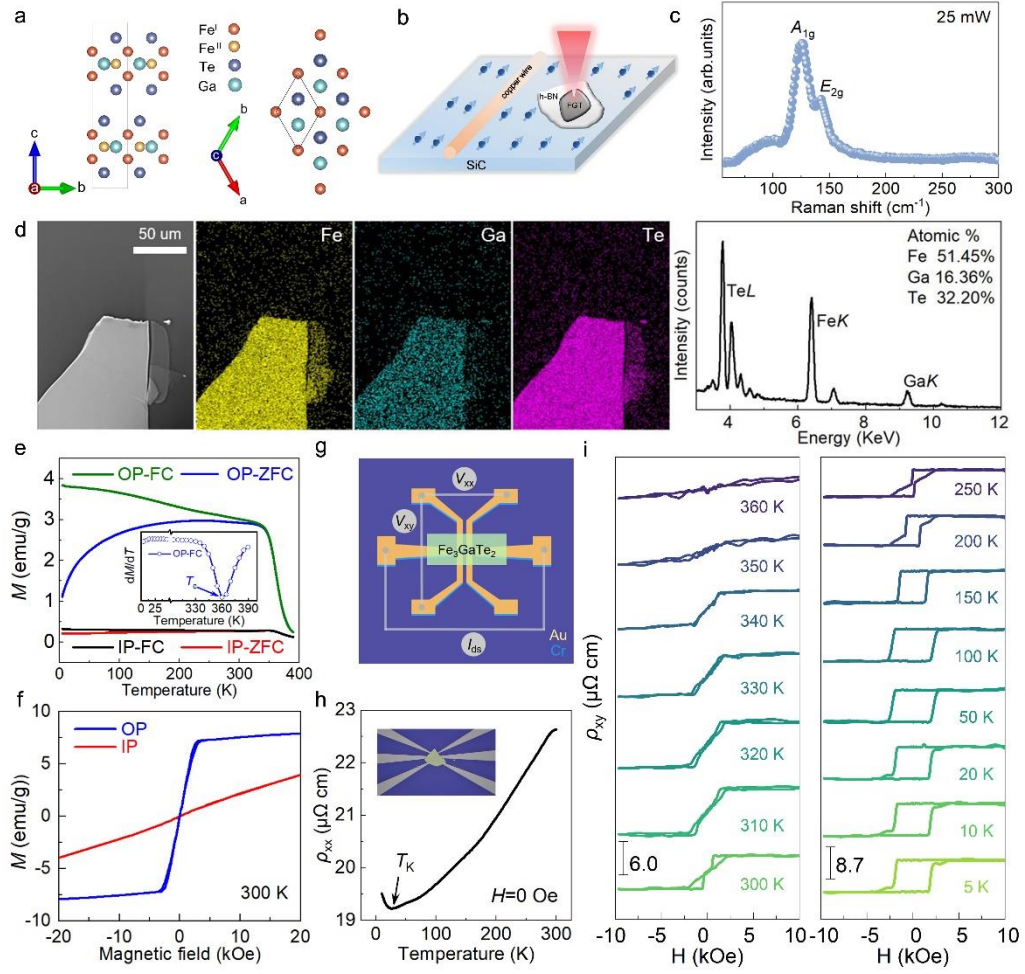


Fig. 1 Characterizations of RT ferromagnet vdW-layered Fe_3GaTe_2 . **a** Crystal structure of Fe_3GaTe_2 from bc -plane and ab -plane views. **b** Schematic of an $\text{hBN}/\text{Fe}_3\text{GaTe}_2$ heterostructure transferred onto SiC , where shallow divacancy defects are used for magnetic detection. **c** Raman spectrum of Fe_3GaTe_2 . **d** SEM image of an exfoliated Fe_3GaTe_2 flake on SiO_2/Si substrate with its corresponding EDS spectrum and EDS mapping of Fe, Ga and Te atoms. **e** Temperature-dependent OP and IP magnetization curves of Fe_3GaTe_2 under ZFC and FC (1000 Oe) conditions, and the inset shows the obtained T_c using temperature-dependent dM/dT curve under OP-FC condition. **f** At 300 K, OP and IP M - H curves of Fe_3GaTe_2 . **g** Schematic diagram of the Fe_3GaTe_2 Hall bar device. **h** Temperature-dependent longitudinal resistivity of the Fe_3GaTe_2 Hall bar device, where T_K represents the Kondo temperature. **i** Temperature-dependent anomalous Hall resistivity of the Fe_3GaTe_2 Hall bar device under OP magnetic field.

at ~ 20 K, indicating the presence of Kondo scattering^{31,32}. Additionally, the OP magnetic field-dependent ρ_{xy} at the temperatures ranging from 5 K to 360 K in Fig. 1i. reveals near-square hysteresis loops, where discontinuous magnetization switching may originate from the multi-domain magnetic structures³³. These characterization results again indicate the large PMA and high T_c of Fe_3GaTe_2 . The above-mentioned

structural, magnetic or electronic transport measurements reveal the good crystalline quality, robust RT ferromagnetism and large PMA of the vdW-layered Fe_3GaTe_2 , making it an ideal RT ferromagnet for low-dimensional spintronic and electronic devices.

After characterizing the basic physical properties of the Fe_3GaTe_2 , we then perform the noninvasive local magnetic detection of it using the PL6 divacancies in 4H-SiC. There are seven types of divacancies (PL1 to PL7) in 4H-SiC, and their spin state S is 1^{34} . The zero-phonon line (ZPL) and zero field splitting (ZFS) D value of PL6 divacancy spins are 1038 nm^{28} and 1351 MHz^{35} , respectively. Its direction is along the c -axis of the 4H-SiC. The schematic of SiC magnetic detection of the Fe_3GaTe_2 sample

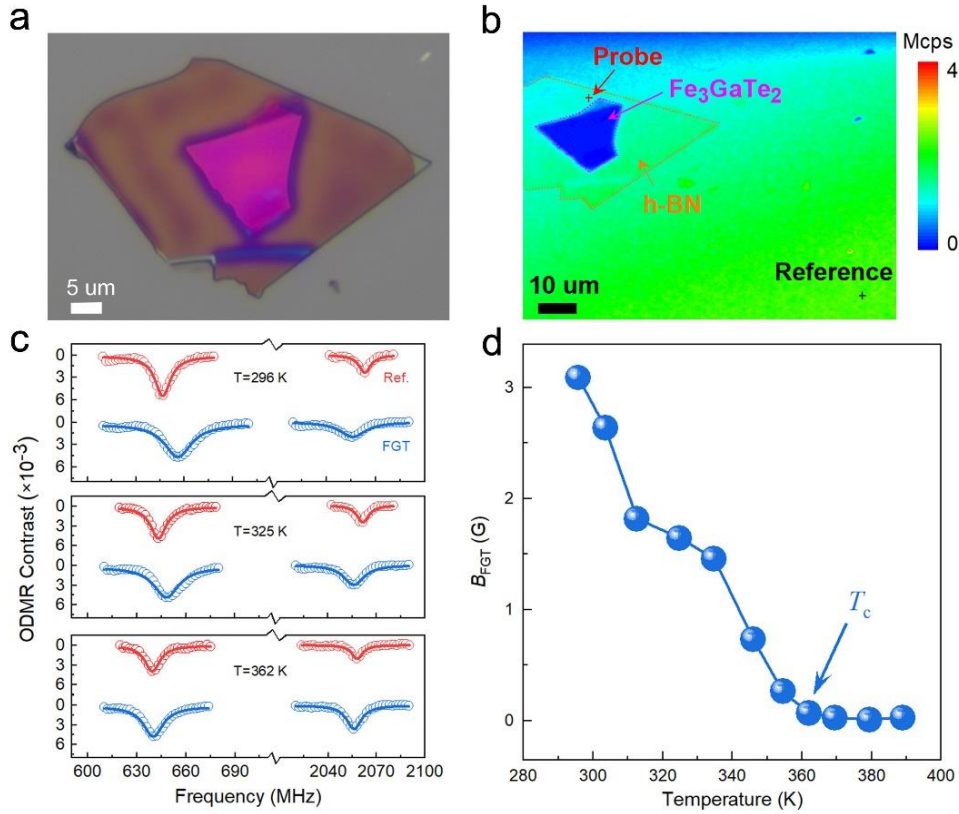


Fig. 2 Magnetic detection of the Fe_3GaTe_2 with temperature. **a** Image of the Fe_3GaTe_2 sample under an optical microscope. The large brown substance covering the Fe_3GaTe_2 (pink sample) is hBN. **b** Confocal scanning microscopy image of the Fe_3GaTe_2 sample. Orange lines outline the boundary of hBN, within which the deep blue area represents the Fe_3GaTe_2 sample, in agreement with optical image. The red and black crosses near and far away from Fe_3GaTe_2 represent the probe position and reference position, respectively. **c** ODMR measurements at the probe position and at the reference position under different temperatures and a magnetic field of $\sim 200 \text{ G}$. Hollow dots are experimental data and the solid lines are the corresponding Lorentz fits. **d** The magnetic fields of Fe_3GaTe_2 B_{FGT} as a function of temperature. From the experiments, we obtain the T_c is $\sim 360 \text{ K}$.

is presented in Fig. 1b. A small flake of Fe_3GaTe_2 is placed on the surface of the SiC, where a shallow layer of PL6 divacancy spins is used to detect the Fe_3GaTe_2 sample. A hBN flake is placed on Fe_3GaTe_2 to protect it from oxidation. First, the temperature-dependent magnetization of the Fe_3GaTe_2 is investigated using the ODMR methods. Figs. 2a. and 2b. show the optical microscopy image and confocal scanning image of the Fe_3GaTe_2 sample, respectively. As shown in Fig. 2b, the probe position (red cross) is close to Fe_3GaTe_2 sample and the reference position (black cross) is far away from the sample.

We perform the ODMR measurements as a function of temperature with a c -axis external magnetic field B_0 of ~ 200 G. For clarity, we define the B_{tot} and B_{FGT} as the total and Fe_3GaTe_2 magnetic fields, respectively. Inferred from the ODMR splitting at the probe and reference positions, we can obtain the corresponding B_{tot} and B_0 , respectively. Then the magnetic field of Fe_3GaTe_2 sample B_{FGT} is $|B_{\text{tot}} - B_0|^{12,13,25,36}$. Fig. 2c. shows three pairs of ODMR results at the probe position and the reference position under different temperatures. The difference values between the probe and reference positions obviously decrease with increasing temperature. In addition, all the ODMR peak values decrease as the temperature increases due to the decrease of the ZFS D^{37} . The inferred B_{FGT} with respect to temperature is displayed in Fig. 2d. The B_{FGT} decreases from about 3.2 G to about 0 G as the temperature increases from 295.8 K to about 360 K, and then remains at about 0 G as the temperature continues to increase to about 389 K. Inferred from the experiments, the T_c of Fe_3GaTe_2 is ~ 360 K, which is consistent with previous results⁹.

In addition to temperature, the external magnetic field also affects the magnetism of the 2D vdW $\text{Fe}_3\text{GaTe}_2^{9,10}$. We then perform ODMR measurements under different external magnetic fields at RT to investigate the relationship between B_{FGT} and the external magnetic field. The confocal scanning microscopic image of the PL6 and Fe_3GaTe_2 is shown in Fig. 3a. We then study the ODMR at the probe position near the Fe_3GaTe_2 (blue cross) and the reference position (black cross). Fig. 3b. presents three pairs of the ODMR measurement results. Both the difference values of the ODMR left and right branches between the reference and probe positions increase as the external magnetic field increases, which means that the B_{FGT} at the probe position increases with increasing external magnetic field. At the same time, we also measure the ODMR under different negative magnetic fields. Fig. 3c. summarizes the B_{FGT} as a function of external magnetic field, and B_{FGT} increases with increasing positive and negative

magnetic field. Inferred from the experiments, we obtain the coercive field of this sample to be ~ 10 G, which is consistent with the $M-H$ curve in Fig. 1f.

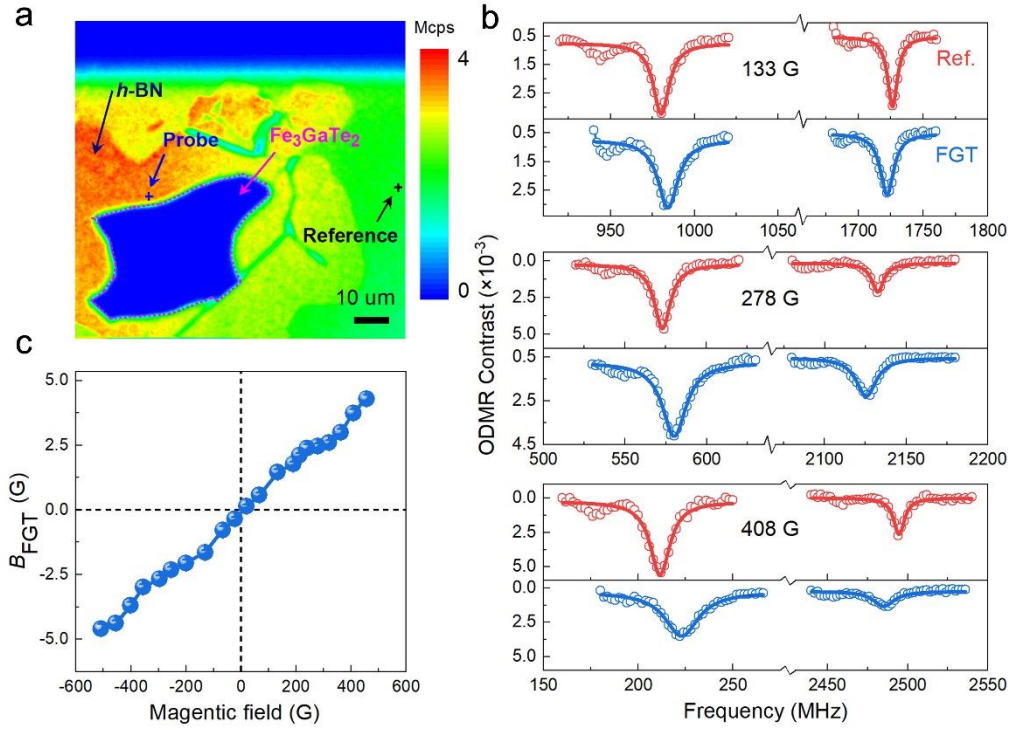


Fig. 3 Magnetic detection of the Fe₃GaTe₂ sample with external magnetic field. **a** Confocal scanning microscopy image of SiC surface, where the blue and black crosses represent the probe position and the reference position, the deep blue polygon is the Fe₃GaTe₂ sample and the rectangular dark blue area at the top of the image is the copper wire. **b** ODMR measurements at the probe position and the reference position under three representative external magnetic fields at RT. The hollow dots are the experimental data and the solid lines are Lorentz fits. **c** B_{FGT} at the probe position as a function of external magnetic fields ranging from -508 G to 455 G.

Except for the static magnetic field, the vdW ferromagnet Fe₃GaTe₂ also exhibits intrinsic dynamic fluctuating magnetic field^{4,5,9,10,12,13}. Unlike traditional magnetic detection methods, as a versatile magnetic quantum sensor, spin defects in SiC could detect both the d.c. and a.c. magnetic fields^{4,5,9,10,12,13,36}. To understand the dynamical behavior of magnetic spin fluctuations generated by static longitudinal magnetic susceptibility and diffusive spin transport of the Fe₃GaTe₂^{12,13,36}, we study the spin relaxometry of PL6 divacancy spins close to the Fe₃GaTe₂ at different temperatures. The upper panel of Fig. 4a. shows the pulse sequence of the divacancy relaxation measurements^{12,13,16}. Three representative PL6 relaxometry results at the reference position under an external magnetic field of ~ 190 G are displayed in the lower part of

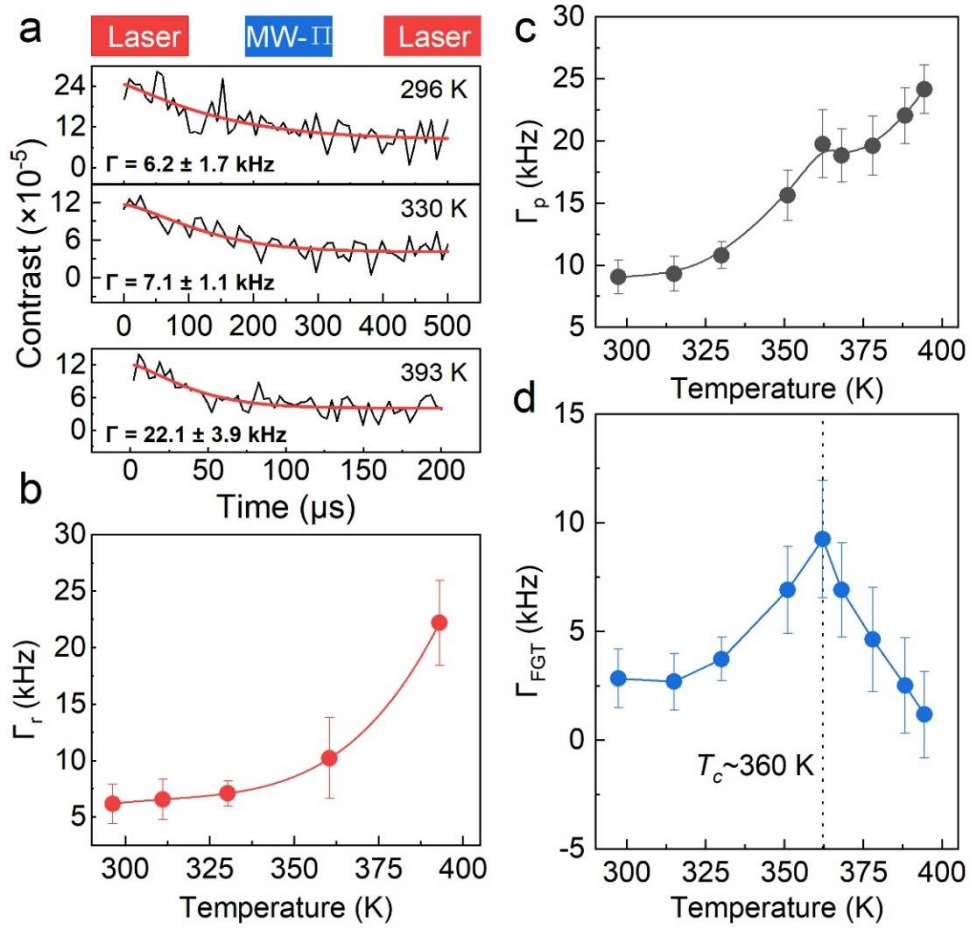


Fig. 4 Fe₃GaTe₂ magnetic spin fluctuation detection using spin relaxometry of PL6. **a** The spin relaxometry pulse sequence and three measurement results at the reference position under different temperatures. As the temperature increases from 296 K to 393 K, the relaxation rate increases from 6.2 kHz to 22.1 kHz. The black lines are experimental data and the red solid lines are the fits to the data. **b**, **c** Summarization of the relaxation rate from RT to 393K at the reference position (**b**) and at the probe position (**c**). The red solid line is the fit. **d** Temperature-dependent relaxation rate of the Fe₃GaTe₂ magnetism, which exhibits a peak around T_c .

Fig. 4a, respectively. We use an exponential decay function $e^{-(t\Gamma)^n}$ to fit the data, where Γ is the relaxation rate and n is the exponential parameter^{12,13,16}. The relaxation rate at RT (296 K) is 6.2 ± 1.7 kHz, which is in agreement with previous results¹⁶. We denote the PL6 relaxation rates at the probe and reference positions (see Supplementary Information Figure 3 for details) as Γ_p and Γ_r , and the derived Fe₃GaTe₂ sample Γ_{FGT} is $\Gamma_p - \Gamma_r$ ^{12,13,16}. It can be seen that the intrinsic relaxation rate Γ_r is larger at higher temperature. Fig. 4b. summarizes the intrinsic relaxation rate Γ_r at the reference position as a function of temperature. It is obvious that Γ_r accelerates its increase with increasing temperatures, which is consistent with previous results of NV center in diamond³⁸.

Given the temperature-dependent effect of higher-energy lattice phonons two-phonon Raman process and the local phonons two-phonon Orbach-type process in SiC³⁸, we fit the data with formular: $\Gamma_r = \mathbf{a} + \mathbf{b}/(\mathbf{e}^{\Delta/kT} - \mathbf{1}) + \mathbf{cT}^5$, where a, b and c are fitting parameters and a is related to PL6 and its spin bath concentration. The k is Boltzmann's constant, T is temperature and Δ is the dominant local vibrational energy³⁸.

As a comparison, we then detect PL6 relaxation rate Γ_p at the probe position under different temperatures. Fig. 4c. exhibits the measured Γ_p at different temperatures. The Γ_p increases faster as the temperature is closer to the T_c of ~ 360 K, and increases slowly as the temperature further increases. By subtracting the intrinsic spin relaxation rate Γ_r at the corresponding temperatures, we can derive the Γ_{FGT} . Fig. 4d. summarizes the temperature-dependent Γ_{FGT} . The magnetic fluctuation rate Γ_{FGT} increases as the temperature increases close to the T_c of ~ 360 K, due to the increase of the magnetic susceptibility around the T_c ^{9,10,12,13}. However, the Γ_{FGT} decreases as the temperature further increases to about 393 K, which is due to the fact that the remaining active magnetic susceptibility decreases and the magnetic fluctuations in Fe₃GaTe₂ are small when temperature exceeds the T_c ^{9,10,12,13}. The phenomenon that temperature-dependent Γ_{FGT} reveals a peak around the T_c is similar to the other vdW ferromagnets and moiré magnetism^{12,13}.

Discussion

In conclusion, we realize the noninvasive static and dynamic fluctuating magnetic detection of 2D vdW RT ferromagnet Fe₃GaTe₂ using PL6 divacancy spins in SiC. Through the temperature- and magnetic field-dependent ODMR measurements near the Fe₃GaTe₂ sample, results show that the T_c is ~ 360 K and the magnetic susceptibility increases with the increasing external magnetic field. Employing spin relaxometry technology, the magnetic spin fluctuations of Fe₃GaTe₂ exhibit a peak around the T_c of ~ 360 K. The versatile PL6 quantum sensor could also be applied to detect the local magnetism of other novel magnetic materials, such as antiferromagnetic materials, superconductors and topological insulators. Combined with infrared CMOS camera^{5,12,13} and SiC anvil cell^{24,29,36,39}, it could realize the magnetic image and magnetic detection of various novel magnetic materials under high pressure. The experiments highlight the significant potential of well-established technologies of SiC spin defects for noninvasive *in situ* investigation of local static and dynamic magnetic behavior in vdW ferromagnets, which could accelerate the development of vdW

ferromagnet-based spintronic and electronic devices.

Methods

Sample and device fabrication

The intrinsic vdW-layered Fe₃GaTe₂ crystal is purchased from Nanjing Mknano Tech. Co., Ltd. For the Fe₃GaTe₂ Hall bar device, pre-patterned Cr/Au (8 nm/50 nm) electrode with a standard Hall bar geometry is fabricated on a SiO₂/Si substrate using lithography technology, thermal evaporation and lift-off technology (see Supplementary Information Figure 2 for details). Therewith, the Fe₃GaTe₂ nanoflakes are mechanically exfoliated with the aid of scotch tape from the bulk counterpart and transferred onto the SiC or SiO₂/Si substrate by polydimethylsiloxane (PDMS) using transfer system, which are performed in the glove box. To avoid the oxidation of Fe₃GaTe₂ sample, a hBN flake is transferred onto the Fe₃GaTe₂ flake to cover and protect.

Physical properties characterizations

Atomic force microscopy and MFM (Bruker) are used to characterize the thickness and magnetic domain structures of the vdW-layered Fe₃GaTe₂. The vibration modes are confirmed by Raman spectroscopy test platform (532 nm solid-state laser, 25 mW excitation Laser). The composition and stoichiometric ratio are obtained by SEM equipped with EDS (JSM-IT500HR). The magnetic properties under various temperatures and magnetic field orientations are performed by superconducting quantum interference device (SQUID, Quantum Design). The ρ_{xx} and ρ_{xy} at different temperatures are detected by an electronic transport measurement system (Model ET9007 from East Changing Technologies, China). During the measurement of ρ_{xy} , the magnetic field is applied perpendicular to the sample and the temperatures ranging from 5 K to ~360 K.

SiC sample and the experimental set-up

The SiC sample is a high-purity 4H-SiC epitaxial layer sample²³. We use the nitrogen ion implantation (energy 30 keV, dose 1×10^{14} cm⁻²) to generate a shallow layer of divacancy ensemble (about 40 nm, stopping and range of ions in matter (SRIM)). Then the sample is annealed at 1050 °C for 2 hours to efficiently generate divacancy centers²³. In the PL6 divacancy magnetic detection experiments, we used a homemade confocal system combined with microwave and magnetic field systems. A 914 nm laser is used

to polarize and read out the divacancy center spin state. A 980 nm dichroic mirror is applied to reflect the laser and an infrared objective (NA=0.65) is utilized to focus the laser on SiC. The PL6 fluorescence is collected by the same objective and transferred to a photoreceiver (Femto, OE-200-IN1) through an optical fiber. We use a 50 μm copper wire for microwave transmission to manipulate PL6 spin state. We use a standard lock-in measuring method to detect spin signal in the experiments^{16,23,25,34}. A metal ceramic heater (HT24S, Thorlabs) and a platinum resistive temperature sensor (TH100PT, Thorlabs) are employed to control and calibrate SiC sample temperature²⁸.

References

1. Burch, K. S., Mandrus, D. & Park, J. G. Magnetism in two-dimensional van der Waals materials. *Nature* **563**, 47-52 (2018).
2. Tokura, Y., Yasuda, K. & Tsukazaki, A. Magnetic topological insulators. *Nat. Rev. Phys.* **1**, 126-143 (2019).
3. Gor'kov, L. P. & Kresin, V. Z. Colloquium: high pressure and road to room temperature superconductivity. *Rev. Mod. Phys.* **90**, 011001 (2018).
4. Casola, F., van der Sar, T. & Yacoby, A. Probing condensed matter physics with magnetometry based on nitrogen-vacancy centres in diamond. *Nat. Rev. Mater.* **3**, 17088 (2018).
5. Xu, Y., Zhang, W. & Tian, C. Recent advances on applications of NV⁻ magnetometry in condensed matter physics. *Photo. Res.* **11**, 393 (2023).
6. Gong, C. et al. Discovery of intrinsic ferromagnetism in two-dimensional van der Waals crystals. *Nature* **546**, 265-269 (2017).
7. Liang, S. J., Cheng, B., Cui, X. Y. & Miao, F. Van der Waals Heterostructures for High-Performance Device Applications: Challenges and Opportunities. *Adv. Mater.* **32**, 1903800 (2019).
8. Bonilla, M. et al. Strong room-temperature ferromagnetism in VSe₂ monolayers on van der Waals substrates. *Nat. Nano.* **13**, 289-293 (2018).
9. Zhang, G. J. et al. Above-room-temperature strong intrinsic ferromagnetism in 2D van der Waals Fe₃GaTe₂ with large perpendicular magnetic anisotropy. *Nat. Commun.* **13**, 5067 (2022).
10. Hu, G. J. et al. Room-Temperature Antisymmetric Magnetoresistance in van der Waals Ferromagnet Fe₃GaTe₂ Nanosheets. *Adv. Mater.* 2403154 (2024).
11. Yang, H. et al. Two-dimensional materials prospects for non-volatile spintronic

- memories. *Nature* **606**, 663-673 (2022).
12. Huang, M. et al. Wide field imaging of van der Waals ferromagnet Fe₃GeTe₂ by spin defects in hexagonal boron nitride. *Nat. Commun.* **13**, 5369 (2022).
 13. Huang, M. et al. Revealing intrinsic domains and fluctuations of moiré magnetism by a wide-field quantum microscope. *Nat. Commun.* **14**, 5259 (2023).
 14. Wang, H. et al. Noninvasive measurements of spin transport properties of an antiferromagnetic insulator. *Sci. Adv.* **8**, eabg8562 (2022).
 15. Bjattacharyya, P. et al. Imaging the Meissner effect in hydride superconductors using quantum sensors. *Nature* **627**, 73-79 (2024).
 16. Koehl, W. F., Buckley, B. B., Heremans, F. J., Calusine, G. & Awschalom, D. D. Room temperature coherent control of defect spin qubits in silicon carbide. *Nature* **479**, 84-87 (2011).
 17. Christle, D. J. et al. Isolated electron spins in silicon carbide with millisecond coherence times. *Nat. Mater.* **14**, 160–163 (2015).
 18. Widmann, M. et al. Coherent control of single spins in silicon carbide at room temperature. *Nat. Mater.* **14**, 164–168 (2015).
 19. Castelletto, S., Lew, C. T-K., Lin, W. X. & Xu, J. S. Quantum systems in silicon carbide for sensing applications. *Rep. Prog. Phys.* **87**, 014501 (2024).
 20. Luo, Q. Y. et al. Fabrication and quantum sensing of spin defects in silicon carbide. *Front. Phy.* **11**, 1270602 (2023).
 21. Son, N. T. et al. Developing silicon carbide for quantum spintronics. *Appl. Phys. Lett.* **116**, 190501 (2020).
 22. Castelletto, S. & Boretti, A. Silicon carbide color centers for quantum applications. *J. Phys. Photonics.* **2**, 022001 (2020).
 23. Wang, J. F. et al. Coherent Control of Nitrogen-Vacancy Center Spins in Silicon Carbide at Room Temperature. *Phys. Rev. Lett.* **124**, 223601 (2020).
 24. John, B. S. et al. Nanotesla magnetometry with the silicon vacancy in silicon carbide. *Phys. Rev. Appl.* **15**, 064022 (2021).
 25. Wang, J. F. et al. Magnetic detection under high pressures using designed silicon vacancy centers in silicon carbide. *Nat. Mater.* **22**, 489–494 (2023).
 26. Falk, A. L. et al. Electrically and mechanically tunable electron spins in silicon carbide color centers. *Phys. Rev. Lett.* **112**, 187601 (2014).
 27. Wolfowicz, G., Whiteley, S. J. & Awschalom, D. D. Electrometry by optical charge conversion of deep defects in 4H-SiC. *Proc. Natl. Acad. Sci.* **115**, 7879–83 (2018).

28. Luo, Q. Y. et al. High-sensitivity silicon carbide divacancy-based temperature sensing. *Nanoscale* **15**, 8432–6 (2023).
29. Liu, L. et al. Coherent control and magnetic detection of divacancy spins in silicon carbide at high pressures. *Nano Lett.* **22**, 9943–9950 (2022).
30. Chen, X., Zhang, X. & Xiang, G. Recent advances in two-dimensional intrinsic ferromagnetic materials Fe_3X ($\text{X}=\text{Ge}$ and Ga) Te_2 and their heterostructures for spintronics. *Nanoscale*. **16**, 527-554 (2024).
31. Zhang, G. J. et al. Field-free room-temperature modulation of magnetic bubble and stripe domains in 2D van der Waals ferromagnetic Fe_3GaTe_2 . *Appl. Phys. Lett.* **123**, 101901(2023).
32. Liu, S. H., Hu, S. J., Cui, X. M. & Kimura, T. Efficient thermo-spin conversion in van der Waals ferromagnet FeGaTe . *Adv. Mater.* **36**, 2309776 (2024).
33. Chen, Z. X., Yang, Y. X., Ying, T. P. & Guo, J. G. High- T_c ferromagnetic semiconductor in thinned 3D Ising ferromagnetic metal Fe_3GaTe_2 . *Nano Lett.* **24**, 993-1000 (2024).
34. Falk, A. L. et al. Polytype control of spin qubits in silicon carbide. *Nat. Commun.* **4**, 1819 (2013).
35. Li, Q. et al. Room-temperature coherent manipulation of single-spin qubits in silicon carbide with a high readout contrast. *Nat. Sci. Rev.* **9**, nwab122 (2021).
36. Hsieh, S. et al. Imaging stress and magnetism at high pressures using a nanoscale quantum sensor. *Science* **366**, 1349-1354 (2019).
37. Yan, F. F. et al. Coherent control of defect spins in silicon carbide above 550 K. *Phys. Rev. App.* **10**, 044042 (2018).
38. Jarmola, A., Acosta, V. M., Jensen, K., Chemerisov, S. & Budker, D. Temperature- and Magnetic-Field-Dependent Longitudinal Spin Relaxation in Nitrogen-Vacancy Ensembles in Diamond. *Phys. Rev. Lett.* **108**, 197601 (2012).
39. Li, T. X. et al. Pressure-controlled interlayer magnetism in atomically thin CrI_3 . *Nat. Commun.* **18**, 1303-1308 (2019).

Acknowledgments

This work was supported by National Key Research and Development Program of China (MOST) (Grant No. 2022YFA1405100) and National Natural Science Foundation of China (NSFC) (Grant No. 52172272, 11975221) and Science Specialty Program of Sichuan University (2020SCUNL210).

Competing interests

The authors declare no competing interests.

Additional information

Supplementary information.